

Chapter 5

The evolution of decameter-wide shear zones at the Cap de Creus, NE Spain

Fusseis, F., Handy, M.R.¹

5.1 Abstract

The formation of decameter-wide greenschist-facies shear zones at the Cap de Creus (NE Spain) involves the networking of shear zones on smaller scales and the subsequent homogenization of strain within the limits of these networks. Deformation in the shear zone networks is accommodated by a suite of mechanisms that characterize the brittle-viscous transition such as brittle fracturing, pressure solution/precipitation, dislocation and viscous grain boundary sliding. Our study shows how different deformation mechanisms contribute to different stages of shear zone propagation and interconnection as well as shear zone widening and strain homogenization.

¹This chapter is written in a paper form but is conceptually related to Chapter 4 and therefor shares a common "Geological Background"-section. The reader is recommended to read the previous chapter prior to this one. This chapter is going to be submitted, in a substantially revised form with an own "Geological Background"-section and more focussed, to *Journal of Structural Geology*.

The investigated shear zone networks consist of networked host shear zones (parallel to the later shearing plane) and step-over shear zones (at high angles to the bulk shearing plane) that isolate sigmoidal lozenges of less-deformed country rock. Meter-wide mylonitic host shear zones interconnected laterally by the propagation of precursory brittle step-over shear zones. Fracturing and frictional sliding in these brittle step-over shear zones was transitional to the formation of extremely fine-grained millimeter-wide ultramylonites by synkinematic reactions of biotite and plagioclase. These ultramylonites deformed by viscous grain boundary sliding. Aside of shear zone interconnection, ultramylonitic shear zones and their precursors, brittle fractures, also contribute to shear zone widening by segmenting drags of mylonitic shear zones.

We interpret the transient formation of ultramylonitic shear zones in step-over orientations to result from elevated stresses caused by strain incompatibilities between neighboring, relatively undeformed lozenges. The rotation of step-over shear zones towards the host shear zones in bulk simple shear reduces stresses in step-over shear zones and forces lozenges to deform internally. Maturing shear zones widen and the dominant deformation mechanism changes to combined crystal plastic and grain size sensitive creep in decimeter- to meter-wide shear zones as they become parallel to the host shear zones and strain within the shear zone network is homogenized. Thermometric and piezometric analysis indicate that these processes were active at greenschist-facies temperatures (400-500° C) and averaged differential stresses of $\sim 22,3$ MPa.

5.2 Introduction

Strain localization in shear zones occurs throughout the entire continental crust, from brittle shear zones that may displace the earth's surface down to highly ductile shear zones that are assumed to characterize strain localization in the lower crust and upper mantle (Scholz, 2002 and references therein). Crustal-scale shear zones are often formed by networks of smaller-scale shear zones. Such shear zone networks do also characterize exposed sections of the fossil brittle-viscous transition (BVT, Mitra, 1979, Choukroune & Gapais, 1983, Hobbs et al., 1986, Gapais et al., 1987, Tourigny & Tremblay, 1997).

At the Cap de Creus (NE Spain) most shear zones are interconnected

and form networks from decameter- to kilometer-scales (Carreras, 2001 and references therein). Fousseis et al. (2006) described the evolution of these shear zone networks, from strain localization in decimeter-long fractures (F-type shear zones) via shear zone interconnection and networking to a stage where the strain distribution was homogenized within the shear zone network and decameter-wide mylonitic (M-) shear zones formed, that define the kilometer-scale Northern Shear Belt (Fig. 1 in Fousseis et al., 2006, Carreras, 2001)².

Fousseis & Handy (Chapter 4 of this thesis) showed how decimeter-long fractures (there termed F-type shear zones) contributed to the propagation of isolated mylonitic (M-type) shear zones. According to Fousseis et al. (2006), F-type shear zones and fracturing promoted lateral shear zone interconnection and thereby networking of shear zones. Furthermore, they were essential in shear zone widening, as they truncated drags towards mylonitic shear zones and thereby eased the synthetic rotation and mylonitic overprint of the foliation in the segmented drag (drag truncation process of Fousseis et al., 2006). Where shear zones interconnected laterally and where they widened, ultramylonitic (UM-type) shear zones formed that are macroscopically characterized by a glass-like fault rock. They were found in the prolongations of F-type shear zones, suggesting that ultramylonitic UM-type shear zones formed from precursory F-type shear zones and were exclusively related to shear zone networking and strain homogenization (Figs. 4.1 and 5.1).

Based on the model for the formation of shear zone networks at the BVT developed by Fousseis et al. (2006) this paper complements previous work and illustrates the significance of the individual types of shear zones, which are characterized by the dominance of different deformation mechanisms, during the networking process and during strain homogenization. After illustrating several aspects of the macroscopic appearance of the individual types (F, UM, M) of shear zones within shear zone networks that have not been shown elsewhere, we complement the outcrop-scale work of Fousseis et al. (2006) by microscale observations from UM- and M-type shear zones. We show that the formation of kilometer-scale shear zones at the BVT involved pressure-, temperature- and grain-size sensitive deformation mechanisms. We evaluate

²See App. 1 in Fousseis et al., 2006 for terminology of shear zones and shear zone networks.

how each of them contributed to homogenize strain distribution within the shear zone networks and, by including paleopiezometric- and thermometric data, link the kinematics of networking shear zones to the evolving rheology.

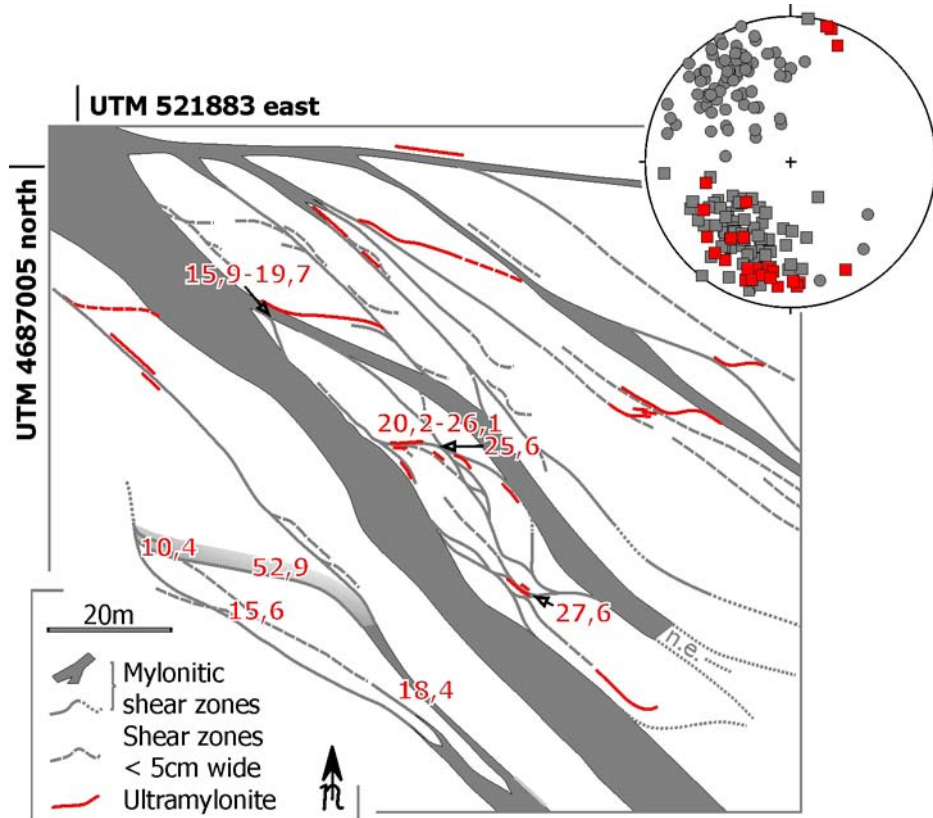


Figure 5.1: Juvenile shear zone network in southern Cala Serena. Lower hemisphere stereonet shows orientation of S3 in mylonitic (M-type) shear zones (gray squares), L3 stretching lineations (gray circles) and *UM-type shear zones* (red squares). Red numbers are paleopiezometric differential stresses during D3 (after Koch, 1983). See fig. 1 in Fusseis et al., 2006 for location. For sample labeling see Fig. 9.4.

5.3 Macroscale observations

5.3.1 F-type shear zones

Fractures (F-type shear zones) form step-over shear zones and are thereby linked to lateral shear zone interconnection (e.g. fig. 3.9 in Fusseis et al., 2006). Within networks of interconnected shear zones, F-type shear

zones are precursors to shear zones that compartmentalize lozenges of less-deformed country rock surrounded by shear zones (e.g. figs. 10 and 11b in Füsseis et al., 2006). Analogous to F-type shear zones in tip damage zones of isolated mylonitic M-type shear zones (Füsseis & Handy, Chapter 4 of this work) fractures within shear zone networks form in damage zones of mylonitic shear zones and are often antithetically deflected with respect to the shearing plane (Fig. 5.2a).

Where F-type shear zones segment drags next to mylonitic shear zones they advance a pronounced synthetic rotation of $S1/2$ in the segments and thereby promote an enhanced mylonitic overprint (Fig. 5.2b). In that way, F-type shear zones allow widening of M-type shear zones (drag truncation of Füsseis et al., 2006). F-type shear zones were found to form the terminations of UM-type shear zones (see below).

5.3.2 UM-type shear zones

In the field, this type of shear zones is characterized by an extremely fine-grained, usually dark-grey to black ultramylonite. Macroscopically, no individual minerals can be resolved in the matrix, with the exception of occasional feldspar clasts. The distribution of UM-type shear zones indicates that this type of shear zones was involved in drag truncation and step-over formation (Fig. 5.1). UM-type shear zones usually emerge from $S3$ (arrow '1' in fig. 9, Füsseis et al., 2006) and were found to terminate as meter-long F-type shear zones. UM-type shear zones are between 2mm and ~ 1 m wide and between 20cm and ~ 10 m long. They occur in macroscopically undeformed metapsammite but also close to mylonitic shear zones or even within them (Figs. 5.3 and 5.4). UM-type shear zones thicker than a few millimeters often show a compositional layering (Fig. 5.4a and b). Occasional shear sense indicators include displaced markers and dragged $S1/2$ (Fig. 5.4b). However, stretching lineations are restricted to dynamically recrystallized quartz-layers in UM-type shear zones.

Narrow, vein-like UM-type shear zones often transect pre-existing fabrics at acute angles without being deflected (Fig. 5.3a). Where truncating drags, millimeter-wide UM-type shear zones usually parallel $S3$ in M-type shear zone centers and are oriented at high angles to $S1/2$ (Fig. 5.3b, stereoplot in Fig. 5.1, cf. orientation of $S1/2$ in fig. 7b of Füsseis et al., 2006). UM-type shear zones form centi- to decimeter wide step-over shear zones parallel or

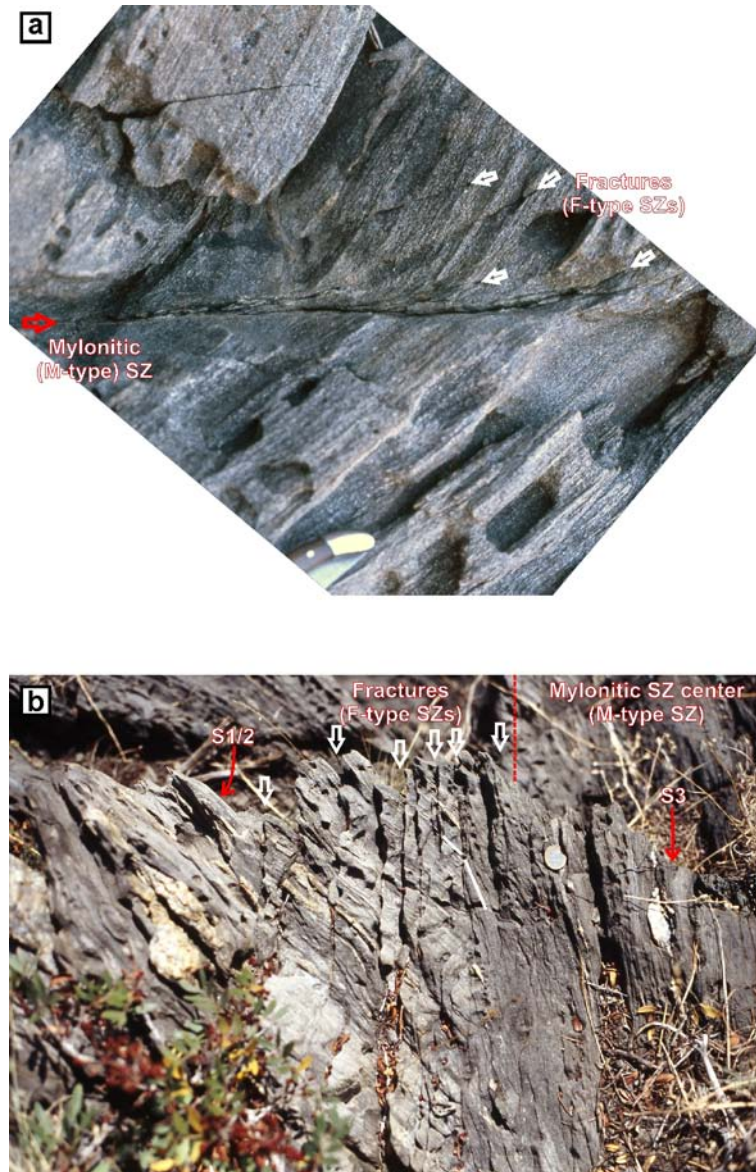


Figure 5.2: F-type shear zones in the Southern Cala Serena SZN. (a) Anticlockwise deflected secondary fractures (white arrows) in the damage zone of a narrow mylonitic shear zone (red arrow). *Laguiole*-knife for scale. View towards the ENE. (b) Fractures truncating the drag alongside a shear zone center (at the right of the image). The fractures are oriented parallel to S3. By segmenting the marginal drag of the shear zone, the fractures promote an enhanced mylonitic overprint of host rock in the segments (Fusseis et al., 2006, note kinked S1/2 - white marker lines). View towards the S. Location of both outcrops shown in Fig. 9.4 in App. 9.5.

at low angles to S1/2 (Fig. 5.4a). The characteristic black seams in the UM-type shear zones were also observed along lithological boundaries between metapelites and metapsammites that usually parallel S1/2 (Fig. 5.3c). No indications for shearing or fracturing were found along these lithological boundaries, indicating that UM-fabrics do not exclusively form in association with precursory F-type shear zones.

S1/2 and other pre-existing fabrics in their foot- and hanging walls are often significantly misoriented across UM-type shear zones which indicates remarkable rotational strains (Fig. 5.4a, see stereoplot in Fig. 9 in Füsseis et al., 2006 for fabric misorientations). The displacement of a marker layer in a thin section of sample CC32 indicates shear strains >30 in a 2mm-wide UM-type shear zone.

Boundaries with the host rock are usually knife-sharp and strain gradients across boundaries of UM-type shear zones are high (Fig. 5.4b, note sheared quartz-vein to the right of the image). If drags towards the shear zones are existent, they are narrow (Fig. 5.4b). Much more often, S1/2 shows sharp cut-offs towards UM-type shear zones (Fig. 5.4c). UM-type shear zones often form discrete boundary layers between M-type shear zone centers and their marginal drags (Fig. 5.4c). UM-type shear zones were also found as millimeter-thick layers within mature mylonitic M-type shear zones.

5.3.3 M-type shear zones

M-type shear zones comprise all first-order shear zones in the Northern Shear Belt and most of the smaller ones and occur in both, host- and step-over orientations (Fig. 5.1). M-type shear zones accommodated the highest displacements within the Cap de Creus shear zone networks and they obtained decameter-width during the advanced stages of shear zone networking (Füsseis et al., 2006). M-type shear zones in the investigated area are 20cm to 20m wide and generally longer than ~ 10 m (Fig. 5.1). Marginal drags have either smooth or sharp cut-offs towards the shear zone center and are often truncated by fractures and UM-type shear zones (Fig. 5.2b, Fig. 5 in Füsseis et al., 2006).

From the marginal drags towards the centers of M-type shear zones a mylonitic foliation (S3) and a pronounced mineral lineation form (L3, Fig. 5.5a). Within shear zone centers lithological variations appear widely ho-

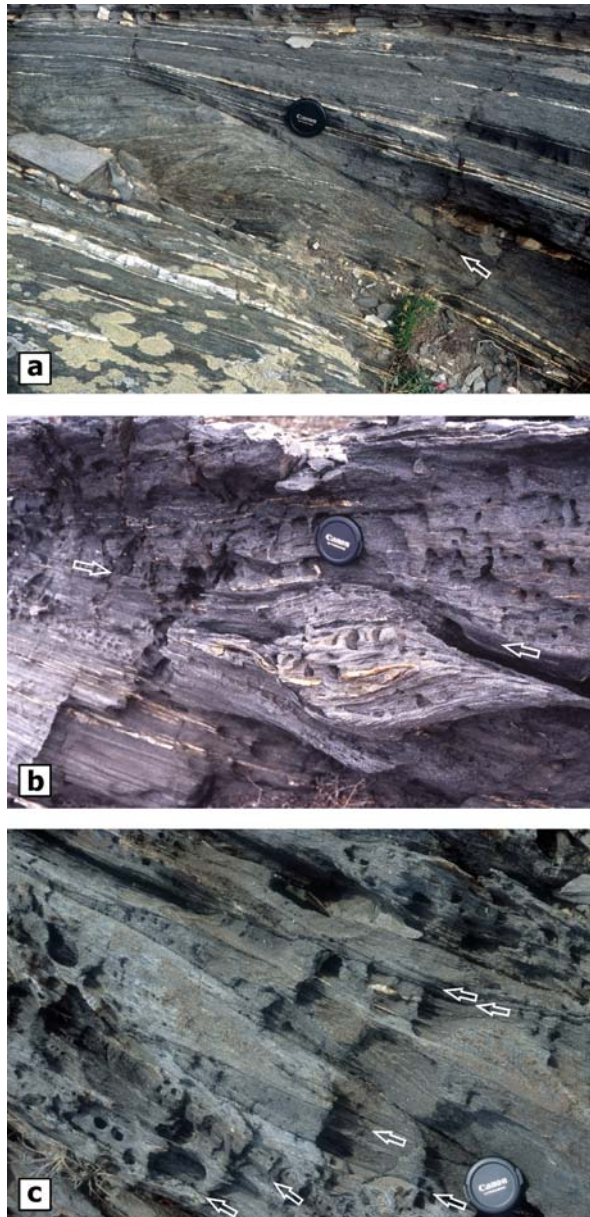


Figure 5.3: UM-type shear zones in the field. (a) Millimeter-wide UM-type shear zone cross-cutting the margins of a mature M-host shear zone. Note that the former emerges from the M-type shear zone. Lens cap 5cm in diameter. View towards the NNE. (b) A UM-type shear zone (white arrows) truncates partly overprinted S2/3 parallel to a M-type shear zone (at the bottom of the photograph). Lens cap 5cm in diameter. View towards the NE. (c) Ultramylonitic layers forming along lithological boundaries (white arrows) between metapsammitic (light in photograph) and metapelitic (dark in photograph) layers, isoclinally folded during D2. Lens cap 5cm in diameter. View towards the SE. Location of all outcrops shown in Fig. 9.4 in App. 9.5.

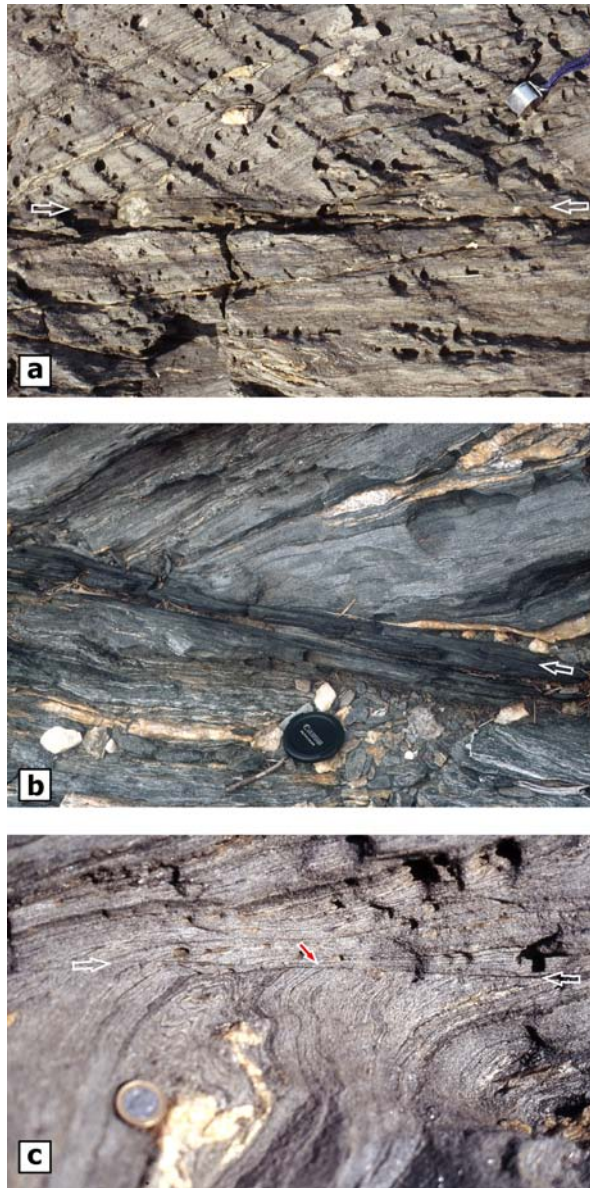


Figure 5.4: UM-type shear zones in the field. (a) Centimeter-wide UM-step-over shear zone (white arrows). Note misorientation of footwall- and hanging wall fabrics. Hand lens for scale. View towards the NNW. (b) Centimeter-wide UM-type shear zone (white arrow). Note sheared quartz-vein at the right margin of the photograph. Foliation in the footwall (S2/3) and hanging wall (S1/2) are significantly misoriented with respect to each other. Lens cap 5cm in diameter. Sampling site of sample CC12. View towards the SE. (c) UM-type shear zone (white arrows) forming the margin to a M-type shear zone (upper half of the photograph). Note continuous, smooth drag towards the M-type shear zone in the left part of the photograph, and sharp cut-offs in the right part (red arrow). Coin diameter 23mm. View towards the ESE. Location of all outcrops shown in Fig. 9.4 in App. 9.5.

mogenized and the grain sizes of the deformed minerals are reduced (Fig. 5.5a). Pre-existing quartz rods and pegmatites are extremely flattened and sheared (Fig. 5.5a&b) and the mylonites appear banded (Fig. 5.5a). Occasional relict folds are isoclinal and their fold axes are rotated parallel to L3 (Carreras et al., 2005). The deflection of S1/2 in marginal drags, SC'-fabrics and centimeter-sized feldspar sigma-clasts indicate top-to-SE shearing along M-type host shear zones and decimeter-wide step-over shear zones (Carreras, 2001, Fousseis et al., 2006). Juvenile (less than several decimeter-wide) M-type step-over shear zones oriented at higher angles to the overall shearing plane may exhibit a top-to-NW or ambiguous sense of shear (Carreras, 2001, Fousseis et al., 2006). In the field, banded M-mylonites clearly differ from the dark-grey, vein-like, glassy appearance of type 2 ultramylonites. However, UM-ultramylonites occur within M-mylonites.

5.4 Microscale observations

Microstructures from F-type shear zones have been described by Fousseis & Handy (Chapter 4 of this work) and are not the subject of this publication. The microstructural description of M-type shear zones in Fousseis & Handy (Chapter 4 of this work) is complemented here. Scanning electron microscopy was done using a JEOL JSM6300 device. Microprobe analyses was carried out with a JEOL 8800 Superprobe with 15kV acceleration voltage and a beam current of 15nA. Natural standards were used for calibration, post-analytical correction was done using the ZAF algorithm. Mineral names used in the text are abbreviated as follows: quartz - Qtz, biotite - Bt, muscovite - Ms, chlorite - Chl, plagioclase - Plag, feldspar - Fsp, Kfsp - K-feldspar, garnet - Grt, apatite - Ap, ilmenite - Ilm, tourmaline - Tur. Supplementary numbering of these abbreviations refers to the generations of these minerals (e.g. Qtz1 - quartz, first generation). For sample descriptions see App. 9.3, for sample locations see Fig. 9.4 in App. 9.5.

5.4.1 Microscale observations from UM-type shear zones

Light- and scanning electron microscopy revealed that the ultramylonites consist of a very fine-grained, laminated, polyphase matrix of distributed Qtz2, Bt2, Plag2, Ms2, Ilm, Chl, newly-grown Grt, an undefined aluminosilicate phase and apatite (Figs. 5.6 and 5.7). Preliminary X-ray fluorescence

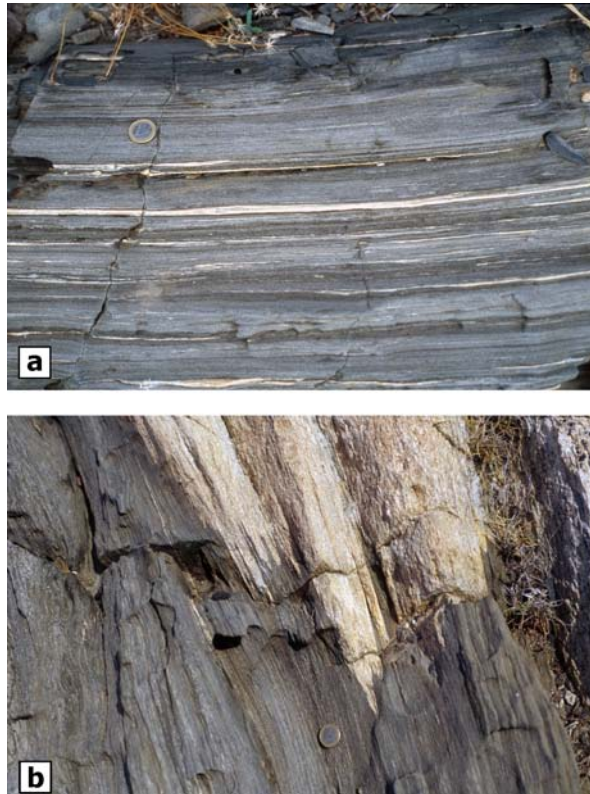


Figure 5.5: M-type shear zones in the field. (a) Banded mylonite in the center of a mature shear zone. Preexistent fabrics are overprinted, Qtz veins are stretched and rolled out. Note plagioclase sigma clasts. Coin diameter 23mm. View towards the E. (b) Contact between a syn-D2 pegmatite and its metapsammitic host rock sheared during D3 and now part of a M-type shear zone. Coin diameter 23mm. View towards the NNW. Location of both outcrops shown in Fig. 9.4 in App. 9.5.

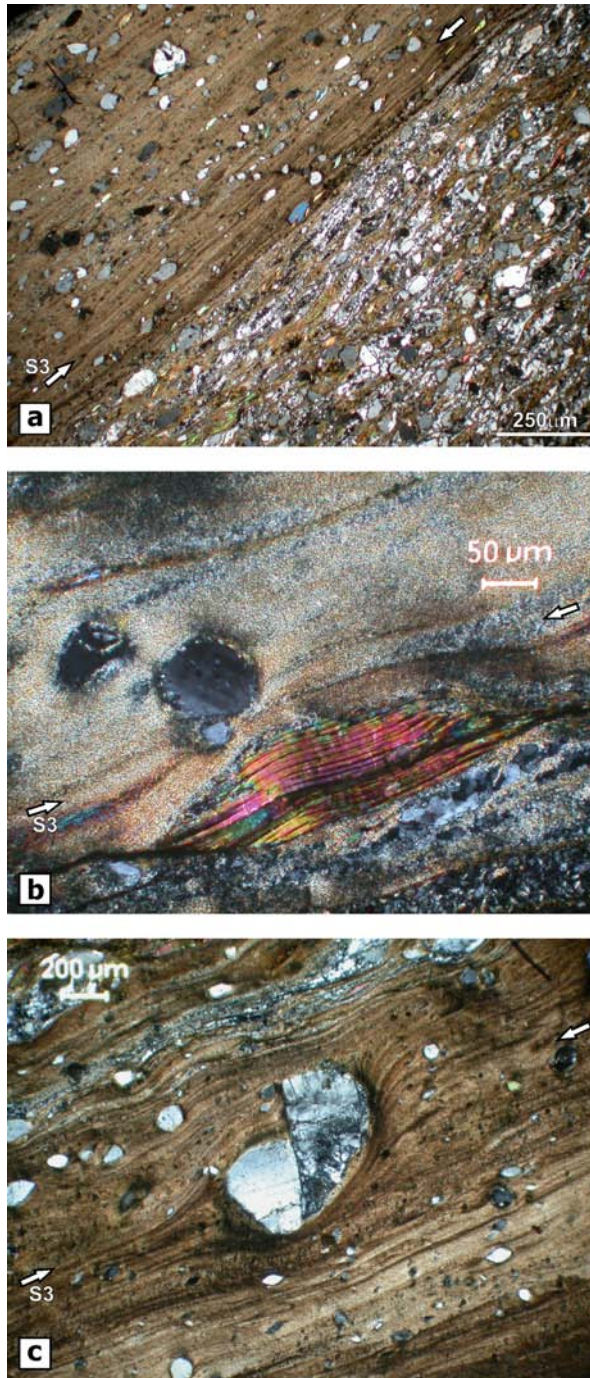


Figure 5.6: UM-type shear zones in thin section. (a) Ultramylonite and its margin towards partly mylonitized host rock. See text for explanation. Sample CC18. (b) Bt porphyroblast in an extremely fine-grained ultramylonitic matrix. Bt is, together with Plag, reacting to form the matrix minerals. See text for explanation. Sample CC17a. (c) Fractured Plag porphyroblast in an ultramylonitic matrix. Sample CC17.

analysis indicate that the bulk compositions of UM-type ultramylonites do not differ significantly from M-type mylonites³. The average grain size of matrix grains is between 4 and 15 μm (samples CC17a&c and CC12a respectively), Grt is usually $<50\mu\text{m}$. Macroscopically visible clasts are up to millimeter-sized Plag1, Bt1 and rare Kfsp1, with Plag1 prevailing. In contrast to porphyroclastic Plag1, porphyroblastic Grt is restricted to specific laminae and tends to be arranged in layers (Fig. 5.7b & 5.8a).

The ultramylonite layers exhibits a compositional banding, individual layers being defined by varying proportions of the above-mentioned secondary minerals (Fig. 5.6a). Within the layers, Bt2, Qtz2 and Plag2 are approximately homogeneously distributed, with occasional clusters of one of the three phases⁴ (Fig. 5.8b&d). While most of the layers are polymineralic, occasional monomineralic layers of dynamically recrystallized Qtz2 occur (Fig. 5.7c). The compositional banding of polyphase and monomineralic layers is parallel to a foliation S3, which is defined by aligned isolated Bt2 and Ilm and the long axes of Qtz2 and Plag2 (Figs. 5.6a&c and 5.8). S3 shows perturbations and is warped around Plag1, Bt1 and Grt clasts (Fig. 5.6c). We interpret this, following observations from delta-clasts (cf. fig. 5.27 in Passchier & Trouw, 2005), as indicating that the clasts rotated. Viewed with crossed polarizers, most Plag1 clasts exhibit strain shadows (Fig. 5.6b).

The outlines of Bt2 in the matrix are often lobate or irregular and are dominated by concave shapes (white arrows in Fig. 5.8c and inset). Long axes of Bt2 aggregates are preferentially oriented at high angles with respect to S3 (Fig. 5.8, S3 indicated by red arrows). Isolated Bt2 flakes are aligned parallel to S3. Bt2/Bt2 grain boundaries are difficult to identify because neighboring Bt2 grains have equal grey-values in SEM-images and the same lattice orientations and therefore no detailed description of their geometry is possible. The basal planes of Bt2 are always aligned parallel to S3 and do not show any features diagnostic of intracrystalline deformation. Qtz2/Bt2 and Plag2/Bt2 phase boundaries show cusps pointing from Bt2 to Qtz2 and Plag2 (white arrows in Fig. 5.8c and inset in d). Cusps tend to be aligned

³Due to restricted sampling, we do not possess enough sample material to quantify the geochemistry of UM-type shear zones any further. However, this is beyond the scope of this paper.

⁴The mineral phase distribution in UM-type ultramylonites is subject of an ongoing investigation.

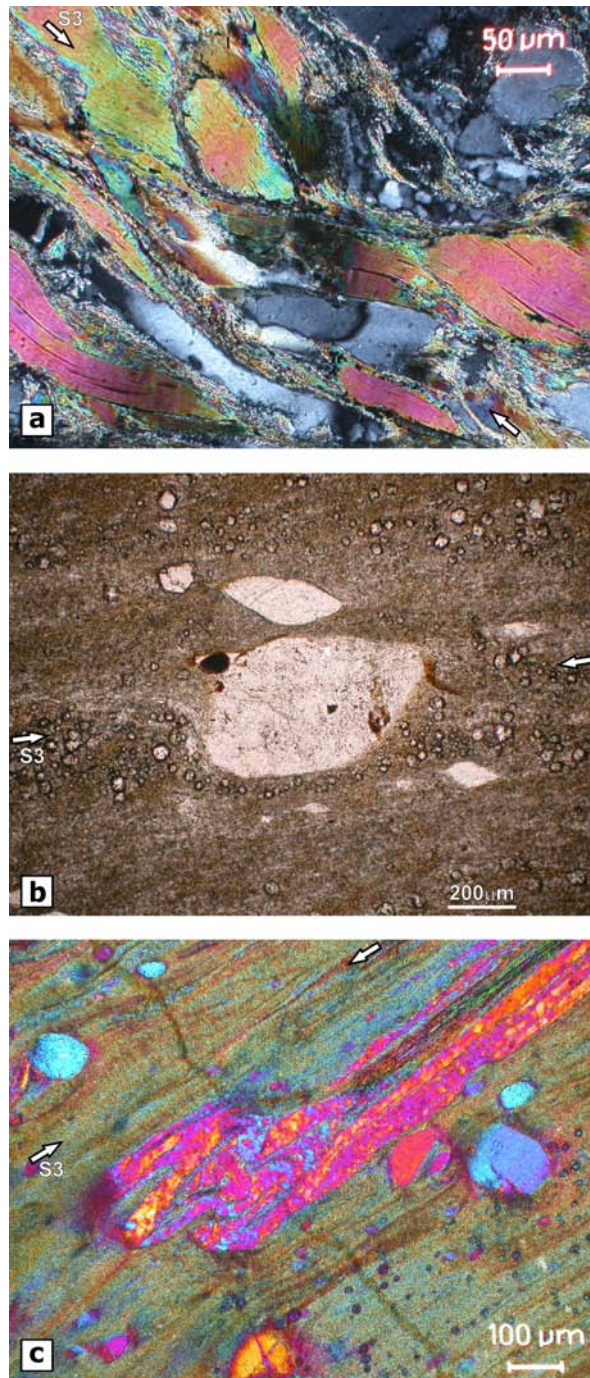


Figure 5.7: Deformation in ultramylonitic samples. (a) Bt1 deforms by solution/precipitation and bending. Note Qtz1 ribbon grains. Sample CC17a. (b) Plag porphyroclast in an ultramylonitic matrix. Minerals with high relief below the porphyroclast are garnets, which are restricted to specific layers. Sample CC12a. (c) Isoclinally folded, dynamically recrystallized Qtz ribbon. Sample CC17a.

parallel to S3. Qtz2 and Plag2 in the ultramylonitic matrix have isometric to elongate shapes. In sample CC12a, which was collected from a ~10cm-wide UM-type shear zone, Qtz2 and Plag2 long axis are aligned in S3 (Fig. 5.8b), whereas in CC17, which comes from a millimeter, vein-like UM-type shear zone, they are randomly oriented (Fig. 5.8c&d). No intracrystalline deformation could be identified in Qtz2 and Plag2 because of their small grain size. Aligned phase- and grain boundaries subparallel to S3 link up along several grain widths in sample CC12a (red lines in Fig. 5.8c).

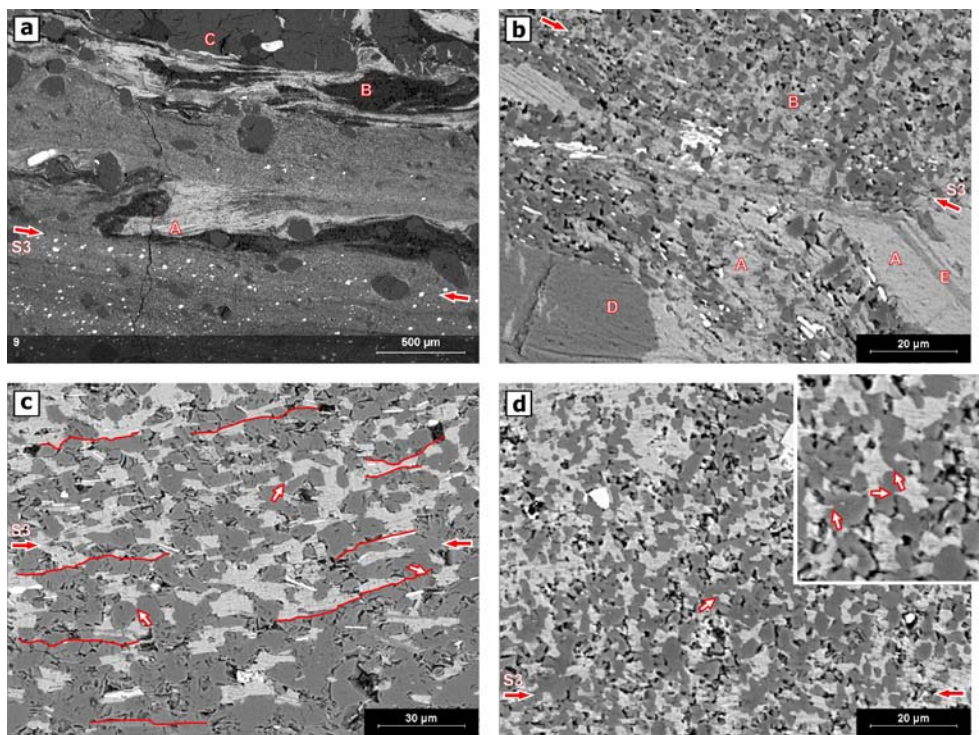


Figure 5.8: SEM photographs of UM-ultramylonites. (a) Ultramylonite in sample CC12. 'A' marks a decaying Bt porphyroblast, 'B' - Qtz, 'C' - Plag. White spots are newly-grown Grt. Sample CC17a. (b) Decaying Bt1 porphyroblast (bottom right corner). Note Chl lamella within the porphyroblast ('E') that can be traced into the recrystallized matrix, indicating the original size of the porphyroblast. 'A' - Bt, 'B' - Qtz2/Plag2, undistinguishable in this picture, 'C' - Kfsp. See Fig. 5.9 for element distribution map. Sample CC17c. (c) Ultramylonitic matrix consisting of Qtz2, Plag2 (both dark grey, undistinguishable in this picture), Bt2 (light grey) and Ilm (white needles). White arrows mark cusps in phase boundaries, indicating interphase boundary migration. Red lines mark inferred intergranular sliding planes. Sample CC12. (d) Ultra fine-grained matrix consisting primarily of Bt2 and Qtz2. White arrows mark cusps in phase boundaries, indicating phase boundary migration (see inset picture). See text for explanation. Sample CC17c.

Monomineralic layers of Qtz2 are formed from dynamically recrystallized Qtz1 ribbons (cf. Figs. 5.7a&c). Qtz1 ribbon grains in country rock adjacent to ultramylonitic layers define S3 throughout the thin section and indicate significant strain prior to ultramylonite formation (Figs. 4.6 in Chapter 4 and 5.7a). Dynamic recrystallization of Qtz1 ribbon grains occurred by subgrain rotation and minor grain boundary bulging. Recrystallized grains show pronounced lattice-preferred- but only minor shape-preferred orientations (Fig. 5.7c). Qtz2 in monomineralic layers grains do not show any signs of static recrystallization. In CC12a one of the ribbons is folded within S3 (Fig. 5.7c). The crystallographic orientations of the recrystallized grains rotate across the hinges of the fold, indicating that recrystallization preceded folding (Fig. 5.8c). The grain size of dynamically recrystallized Qtz2 in monomineralic layers of UM-type shear zones is difficult to measure, but significantly smaller than within M-type shear zones ($\ll 70, 4\mu\text{m}$). Monomineralic quartz layers in UM-type mylonites are not boudinaged, indicating that the syndeformational competency contrast between the polyphase matrix and the recrystallized Qtz2 layers was minor.

Bt1 in UM-type shear zones generally shows evidence for a synkinematic reaction (Figs. 5.8a&b and 5.9). Fig. 5.8b shows a reactant Bt1 grain. Element distributions of this grain were mapped (Fig. 5.9) and indicate that the possible reaction of Bt1 is similar to the retrograde reactions of Bt1 described in Chapter 4 of this thesis: $\text{Bt1} \rightarrow \text{Bt2} + \text{Ms2} + \text{Chl} + \text{Ilm}$. This reaction was described by Kerrich et al. (1980, 1981) as potentially stress-induced and deformation-catalyzed. The mapped Bt1 clast in Fig. 5.9 (see also Fig. 5.8b for detail) is internally undeformed and exhibits a central lamella of Chl (Fig. 5.8b). The lamella can be traced into the recrystallized matrix (white arrow in Fig. 5.8b), indicating the original size of the clast. Along its margins (within the original limits of the clast), Qtz2, Plag2, Ms2, Bt2 and Ilm form a mantle of recrystallized grains (Fig. 5.9). Mineral phase distribution in the immediate vicinity of the clast is remarkably homogeneous (Fig. 5.9).

The SEM image in Fig. 5.10 (right, bottom image) shows a phase boundary between Bt1 and two Plag1 grains. Between the three, fine seams of Qtz2, Ms2 and Ilm indicate that Bt1 and Plag1 react and Ms2, Ilm and Qtz2 are formed (see element distribution mappings in Fig. 5.10). Interestingly, no newly-grown Ca, Na and Mg-bearing phases were found in the

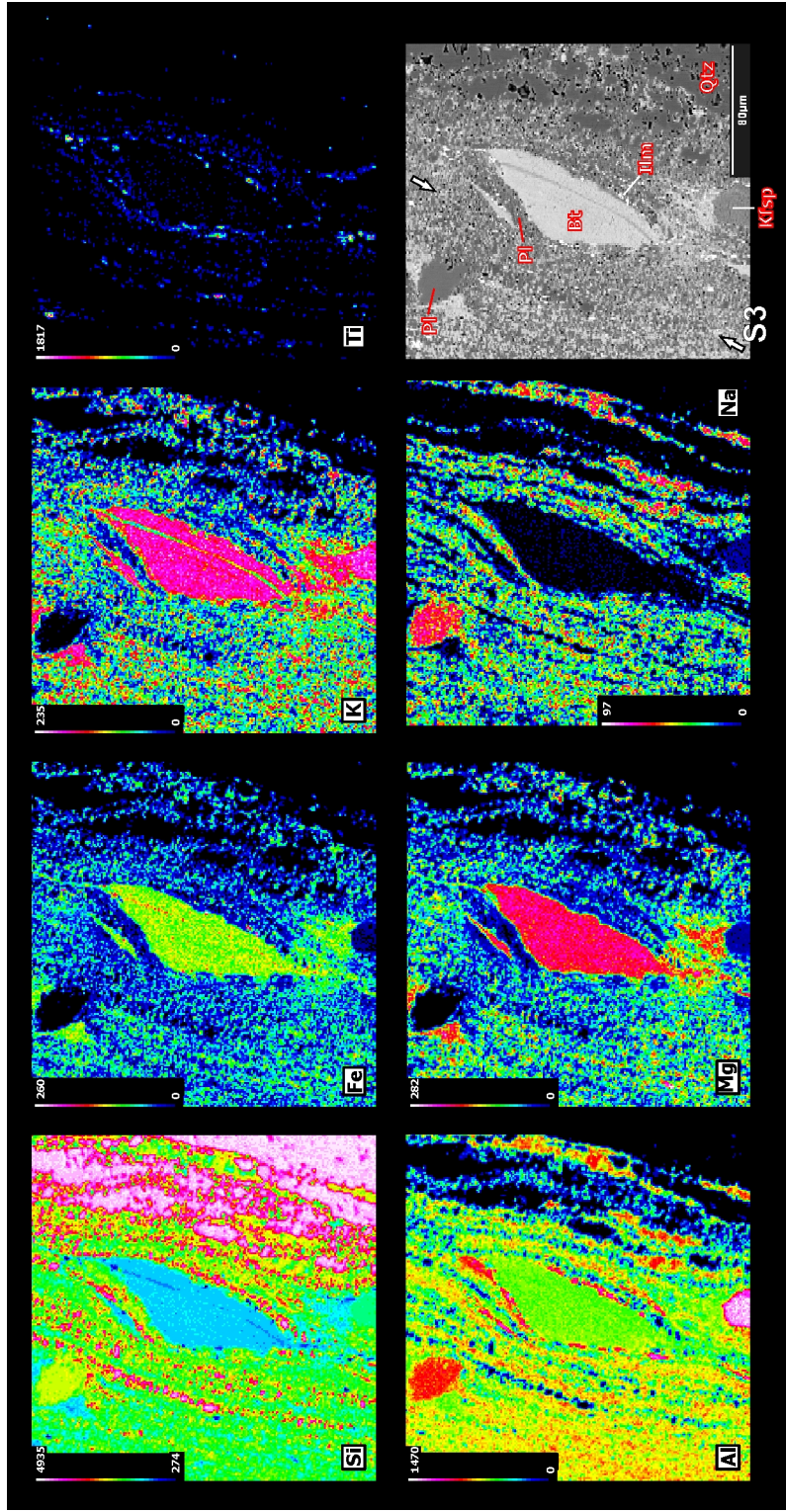


Figure 5.9: Element distribution map of decaying Bt1 porphyroblast (see Fig. 5.8a), indicating the formation of Qtz2, Plag2, Bt2 and Ilm from Bt1. Bottom right corner - BSE image of the mapped site. See text for explanations. Sample CC17a.

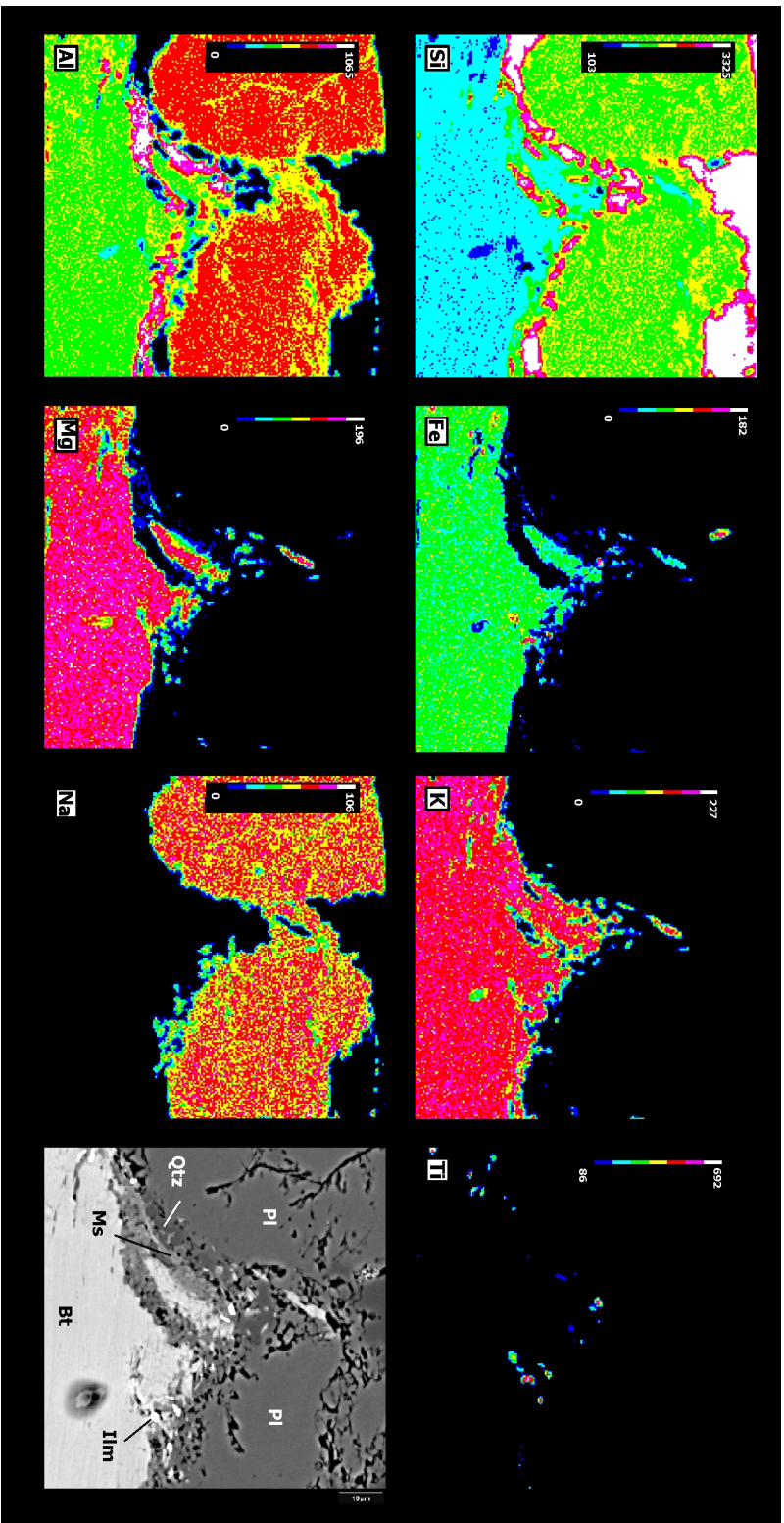


Figure 5.10: Element distribution map from Plag1/Bt1 reaction site. Newly grown Qtz2, Ms2 and Ilm at the reaction site indicate the diffusive evacuation of Ca and Na. Bottom right corner - BSE image of the mapped site. See text for explanations. Sample CC17a.

immediate vicinity of the reaction site. In the same sample, accessory apatite was found to react, with Plag2, Bt2 and Ms2 forming along phase boundaries with Qtz1 ribbon grains. Until today we did not quantify the kinetics of these reactions and further work needs to be done to define the processes that control the decay of Bt1 and Plag1. However, based on the close spatial proximity of the reaction sites to the ultramylonitic layers (e.g. 'A' in Fig. 5.8a) we interpret the ultramylonitic matrix to have been formed by neocrystallized reaction products (see below). This would have included mass transfer on a scale significantly larger than the grain size of the reaction products. In that way the Ca-bearing phases in the ultramylonitic matrix (Grt, Plag2, Ap2) could have consumed Ca resulting from the reaction of Plag1 and Ap1 and K- and Mg-bearing phases could have formed along the grain boundaries of Ap1. Additional evidence for diffusive mass transfer is given by Bt2-filled extension gashes at high angles to S3 in Plag1 (Fig. 5.11).

The margins of ultramylonites towards the host rock may be knife sharp and are then usually parallel to the flow lamination in the ultramylonitic matrix (Fig. 5.6a). However, observations from sample CC17c suggest that the margins originally followed the irregular outlines of primary minerals of the host rock (Qtz1 ribbon grains, Plag1 and Bt1, Fig. 5.11): Outside a central ultramylonitic layer (red arrows in Fig. 5.11), isolated aggregates of fine-grained reaction products next to Bt1 and Plag1 indicate that the ultramylonites forms by interconnection of such aggregates (white arrows in Fig. 5.11).

5.4.2 Geothermometry of UM-type shear zones

The occurrence of Grt porphyroblasts is restricted to the ultramylonitic matrix and we therefore interpret them to have grown synkinematically. In sample CC17a, using an electron microprobe, Grt compositions were measured together with those of isolated matrix Bt2 as well as of Bt1 porphyroblasts. Element distribution mappings of Grt point to a compositional zoning, with Fe- and Mg-rich and Ca-poor cores, surrounded by an Mg-depleted and Ca-enriched rim and an outermost zone with decreased Fe and Ca and increased Mg.

In order to estimate temperature of the last deformation increments rim compositions of Grt and Bt2 compositions from adjacent pressure shad-

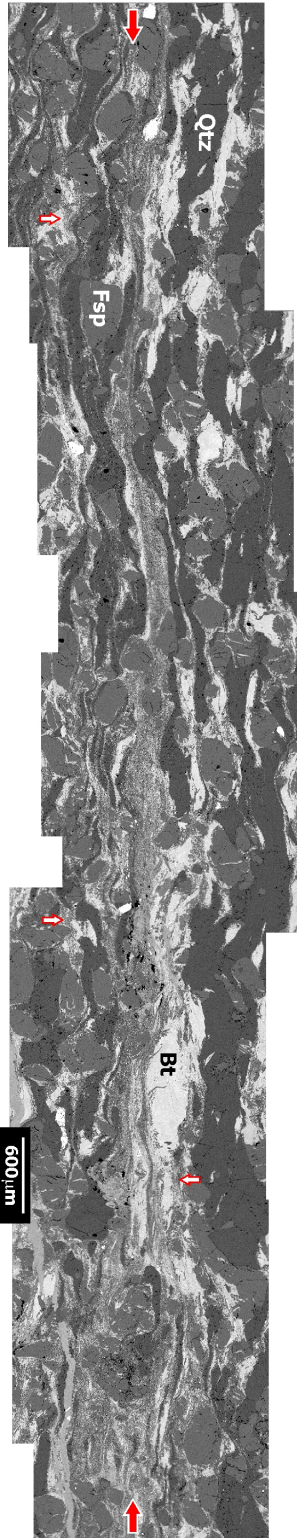


Figure 5.11: SEM photomerge of juvenile UM-type shear zone (red arrows). White arrows mark sites where reacting Bt and Plag form fine-grained aggregates of matrix minerals. See text for explanations. Sample CC17c.

ows (Table 5.2) were used to obtain syndeformational temperatures for Fe-Mg exchange between the two phases (Table 5.1). From the measured compositions temperatures between $461\pm 50^\circ\text{C}$ (Ferry & Spear, 1978) and $495\pm 50^\circ\text{C}$ (Hodges & Spear, 1982) were calculated for pressures of 300-350MPa (Druguet, 2001). Depending on the distance from the actual phase boundary, calculated temperatures varied in the range of about 20-30°C.

Complementary, arbitrarily chosen Bt2/Grt data pairs from isolated measurements gave similar temperatures (Table 5.1). Additionally we applied the recently published Ti-in-biotite thermometer to compositional data from matrix Bt2 and Bt1 clasts (Henry & Guidotti, 2002, Henry et al. 2005). Again, the thermometer was calibrated for syn-D3 pressures of 300-350MPa following Druguet (2001). Ti-in-Bt thermometry yielded $395\pm 25^\circ\text{C}$ for matrix Bt2 and $430\pm 50^\circ\text{C}$ for Bt1 clasts (Fig. 5.12, see App. 9.11 for data), following Henry et al. (2005). The lower temperatures for the Ti-in-Bt thermometer (compare data in Table 5.1) may be indicative of ongoing re-equilibration of Bt2 during progressive cooling of the rocks after passing the closure temperature for Fe-Mg exchange between Grt and Bt2 (Fig. 5.12). Results from both thermometrical calculations correspond to a published temperature interval for D3 between 560°C and 400°C (Druguet, 2001). Since UM-type shear zones are kinematically embedded in the shear zone network (see discussion below), the calculated temperatures are assumed to represent syndeformational temperatures for all types of shear zones.

5.4.3 Microscale observations from M-type shear zones

Strain localization in M-type shear zones was described by Füsseis & Handy (Chapter 4 of this thesis). Deformation in mature M-type shear zones was predominantly accommodated by fine-grained, dynamically recrystallized Qtz2 and a synkinematically formed matrix of Bt2, Ms2, Ilm and Chl resulting from a deformation-induced reaction of Bt1. (Fig. 5.13a&b, Füsseis & Handy, Chapter 4 of this thesis). Average grain sizes in polyphase mylonites are $\sim 50\mu\text{m}$ (Fig. 5.13b&c), only in some of the mica-rich samples the grain size of the neocrystallized matrix becomes smaller than $\sim 25\mu\text{m}$. Aligned secondary mica and Ilm define S3, which is deflected around Plag1 and Ms1 porphyroclasts (Figs. 4.13b). S3 is dragged into top-to-SE shear bands that characterize M-type mylonites (Figs. 4.13a and 5.13a).

In Figs. 5.7a and 5.13a, which show less-deformed mylonites, Qtz1 forms

	Garnet				Biotite				Temp (°C) FS78	Temp (°C) HS82	
	Fe	Mn	Mg	Ca	Ti	AlVI	Fe	Mg			
Line 27 Grt17a	2,228	0,192	0,330	0,195	Line 12 Grt17a 040106_Bt-Grt	0,103	1,166	1,054	1,184	481	506
040106_Bt-Grt					Grt						
Line 29 Grt17a	2,201	0,194	0,321	0,224	Line 11 Grt17a 040106_Bt-Grt	0,107	1,139	1,053	1,211	471	500
040106_Bt-Grt					Grt						
Line 30 Grt17a	2,152	0,178	0,301	0,271	Line 10 Grt17a 040106_Bt-Grt	0,104	1,160	1,030	1,213	454	489
040106_Bt-Grt					Grt						
Line 32 Grt17a	2,175	0,174	0,274	0,285	Line 5 Grt17a 040106_Bt-Grt	0,095	1,025	0,921	1,064	433	469
040106_Bt-Grt					Grt						
Line 33 Grt17a	2,157	0,179	0,287	0,279	Line 3 Grt17a 040106_Bt-Grt	0,098	0,916	0,867	0,909	471	507
040106_Bt-Grt					Grt						
grt17a_161205_21	2,141	0,250	0,298	0,250	Grid 5-10 Grt17a Grid 1	0,111	1,218	1,058	1,174	468	500
grt17a_161205_22	2,002	0,293	0,275	0,397	biot17c_161205_2	0,118	1,097	1,007	1,222	442	491
grt17a_161205_24	2,111	0,310	0,304	0,255	biot17c_161205_5	0,125	1,196	1,056	1,261	458	490
grt17a_161205_27	2,165	0,334	0,331	0,148	biot17c_161205_9	0,089	0,813	0,905	1,063	478	497
Grid 7-5 Grt17a Grid 1	2,089	0,253	0,310	0,238	Grid 14-2 Grt17a Grid 1	0,089	1,047	0,833	0,997	465	496
Grid 5-6 Grt17a Grid 1	2,010	0,280	0,299	0,230	Grid 12-9 Grt17a Grid 1	0,068	0,936	0,944	0,926	521	553
Grid 5-2 Grt17a Grid 1	2,054	0,254	0,273	0,339	Grid 11-10 Grt17a Grid 1	0,084	0,995	0,886	1,036	443	486
Grid 4-8 Grt17a Grid 1	1,977	0,248	0,259	0,381	Grid 9-10 Grt17a Grid 1	0,048	1,112	0,773	1,039	408	456

Table 5.1: Synkinematic temperatures, calculated from Bt and Grt compositions (given in atoms per formula unit) measured in samples CC17a and CC17c using the Bt/Grt thermometer of Ferry & Spear (1978) and Hodges & Spear (1982). See text for explanation and Table 5.2 for representative electron microprobe measurements.

Case	Site	Case
CC17a	Bt1	CC17c
CC17b	Bt2	CC17d
CC17e	Bt3	CC17f
CC17g	Bt4	CC17h
CC17i	Bt5	CC17j
CC17k	Bt6	CC17l
CC17m	Bt7	CC17n
CC17o	Bt8	CC17p
CC17q	Bt9	CC17r
CC17s	Bt10	CC17t
CC17u	Bt11	CC17v
CC17w	Bt12	CC17x
CC17y	Bt13	CC17z
CC17aa	Bt14	CC17ab
CC17ac	Bt15	CC17ad
CC17ae	Bt16	CC17af
CC17ag	Bt17	CC17ah
CC17ai	Bt18	CC17aj
CC17ak	Bt19	CC17al
CC17am	Bt20	CC17an
CC17ao	Bt21	CC17ap
CC17aq	Bt22	CC17ar
CC17as	Bt23	CC17at
CC17au	Bt24	CC17av
CC17aw	Bt25	CC17ax
CC17ay	Bt26	CC17az
CC17ba	Bt27	CC17bb
CC17bc	Bt28	CC17bd
CC17be	Bt29	CC17bf
CC17bg	Bt30	CC17bh
CC17bi	Bt31	CC17bj
CC17bk	Bt32	CC17bl
CC17bm	Bt33	CC17bn
CC17bo	Bt34	CC17bp
CC17bq	Bt35	CC17br
CC17bs	Bt36	CC17bt
CC17bu	Bt37	CC17bv
CC17bw	Bt38	CC17bx
CC17by	Bt39	CC17bz
CC17ca	Bt40	CC17cb
CC17cc	Bt41	CC17cd
CC17ce	Bt42	CC17cf
CC17cg	Bt43	CC17ch
CC17ci	Bt44	CC17cj
CC17ck	Bt45	CC17cl
CC17cm	Bt46	CC17cn
CC17co	Bt47	CC17cp
CC17cq	Bt48	CC17cr
CC17cs	Bt49	CC17ct
CC17cu	Bt50	CC17cv
CC17cw	Bt51	CC17cx
CC17cy	Bt52	CC17cz
CC17da	Bt53	CC17db
CC17dc	Bt54	CC17dd
CC17de	Bt55	CC17df
CC17dg	Bt56	CC17dh
CC17di	Bt57	CC17dj
CC17dk	Bt58	CC17dl
CC17dm	Bt59	CC17dn
CC17do	Bt60	CC17dp
CC17dq	Bt61	CC17dr
CC17ds	Bt62	CC17dt
CC17du	Bt63	CC17dv
CC17dw	Bt64	CC17dx
CC17dy	Bt65	CC17dz
CC17ea	Bt66	CC17eb
CC17ec	Bt67	CC17ed
CC17ee	Bt68	CC17ef
CC17eg	Bt69	CC17eh
CC17ei	Bt70	CC17ej
CC17ek	Bt71	CC17el
CC17em	Bt72	CC17en
CC17eo	Bt73	CC17ep
CC17eq	Bt74	CC17er
CC17es	Bt75	CC17et
CC17eu	Bt76	CC17ev
CC17ew	Bt77	CC17ex
CC17ey	Bt78	CC17ez
CC17fa	Bt79	CC17fb
CC17fc	Bt80	CC17fd
CC17fe	Bt81	CC17ff
CC17fg	Bt82	CC17fh
CC17fi	Bt83	CC17fj
CC17fk	Bt84	CC17fl
CC17fm	Bt85	CC17fn
CC17fo	Bt86	CC17fp
CC17fq	Bt87	CC17fr
CC17fs	Bt88	CC17ft
CC17fu	Bt89	CC17fv
CC17fw	Bt90	CC17fx
CC17fy	Bt91	CC17fz
CC17ga	Bt92	CC17gb
CC17gc	Bt93	CC17gd
CC17ge	Bt94	CC17gf
CC17gg	Bt95	CC17gh
CC17gi	Bt96	CC17gj
CC17gk	Bt97	CC17gl
CC17gm	Bt98	CC17gn
CC17go	Bt99	CC17gp
CC17gq	Bt100	CC17gr
CC17gs	Bt101	CC17gt
CC17gu	Bt102	CC17gv
CC17gw	Bt103	CC17gx
CC17gy	Bt104	CC17gz
CC17ha	Bt105	CC17hb
CC17hc	Bt106	CC17hd
CC17he	Bt107	CC17hf
CC17hg	Bt108	CC17hh
CC17hi	Bt109	CC17hj
CC17hk	Bt110	CC17hl
CC17hm	Bt111	CC17hn
CC17ho	Bt112	CC17hp
CC17hq	Bt113	CC17hr
CC17hs	Bt114	CC17ht
CC17hu	Bt115	CC17hv
CC17hw	Bt116	CC17hx
CC17hy	Bt117	CC17hz
CC17ia	Bt118	CC17ib
CC17ic	Bt119	CC17id
CC17ie	Bt120	CC17if
CC17ig	Bt121	CC17ih
CC17ii	Bt122	CC17ij
CC17ik	Bt123	CC17il
CC17im	Bt124	CC17in
CC17io	Bt125	CC17ip
CC17iq	Bt126	CC17ir
CC17is	Bt127	CC17it
CC17iu	Bt128	CC17iv
CC17iw	Bt129	CC17ix
CC17iy	Bt130	CC17iz
CC17ja	Bt131	CC17jb
CC17jc	Bt132	CC17jd
CC17je	Bt133	CC17jf
CC17jg	Bt134	CC17jh
CC17ji	Bt135	CC17jj
CC17jk	Bt136	CC17jl
CC17jm	Bt137	CC17jn
CC17jo	Bt138	CC17jp
CC17jq	Bt139	CC17jr
CC17js	Bt140	CC17jt
CC17ju	Bt141	CC17jv
CC17jw	Bt142	CC17jx
CC17jy	Bt143	CC17jz
CC17ka	Bt144	CC17kb
CC17kc	Bt145	CC17kd
CC17ke	Bt146	CC17kf
CC17kg	Bt147	CC17kh
CC17ki	Bt148	CC17kj
CC17kk	Bt149	CC17kl
CC17km	Bt150	CC17kn
CC17ko	Bt151	CC17kp
CC17kq	Bt152	CC17kr
CC17ks	Bt153	CC17kt
CC17ku	Bt154	CC17kv
CC17kw	Bt155	CC17kx
CC17ky	Bt156	CC17kz
CC17la	Bt157	CC17lb
CC17lc	Bt158	CC17ld
CC17le	Bt159	CC17lf
CC17lg	Bt160	CC17lh
CC17li	Bt161	CC17lj
CC17lk	Bt162	CC17ll
CC17lm	Bt163	CC17ln
CC17lo	Bt164	CC17lp
CC17lq	Bt165	CC17lr
CC17ls	Bt166	CC17lt
CC17lu	Bt167	CC17lv
CC17lw	Bt168	CC17lx
CC17ly	Bt169	CC17ly
CC17la	Bt170	CC17lz
CC17ma	Bt171	CC17mb
CC17mc	Bt172	CC17md
CC17me	Bt173	CC17mf
CC17mg	Bt174	CC17mh
CC17mi	Bt175	CC17mj
CC17mk	Bt176	CC17ml
CC17mm	Bt177	CC17mn
CC17mo	Bt178	CC17mp
CC17mq	Bt179	CC17mr
CC17ms	Bt180	CC17mt
CC17mu	Bt181	CC17mv
CC17mw	Bt182	CC17mx
CC17my	Bt183	CC17mz
CC17na	Bt184	CC17nb
CC17nc	Bt185	CC17nd
CC17ne	Bt186	CC17nf
CC17ng	Bt187	CC17nh
CC17ni	Bt188	CC17nj
CC17nk	Bt189	CC17nl
CC17nm	Bt190	CC17nn
CC17no	Bt191	CC17np
CC17nq	Bt192	CC17nr
CC17ns	Bt193	CC17nt
CC17nu	Bt194	CC17nv
CC17nw	Bt195	CC17nx
CC17ny	Bt196	CC17ny
CC17na	Bt197	CC17nz
CC17oa	Bt198	CC17ob
CC17oc	Bt199	CC17od
CC17oe	Bt200	CC17of
CC17og	Bt201	CC17oh
CC17oi	Bt202	CC17oj
CC17ok	Bt203	CC17ol
CC17om	Bt204	CC17on
CC17oo	Bt205	CC17op
CC17oq	Bt206	CC17or
CC17os	Bt207	CC17ot
CC17ou	Bt208	CC17ov
CC17ow	Bt209	CC17ox
CC17oy	Bt210	CC17oy
CC17na	Bt211	CC17oz
CC17pa	Bt212	CC17pb
CC17pc	Bt213	CC17pd
CC17pe	Bt214	CC17pf
CC17pg	Bt215	CC17ph
CC17pi	Bt216	CC17pj
CC17pk	Bt217	CC17pl
CC17pm	Bt218	CC17pn
CC17po	Bt219	CC17pp
CC17pq	Bt220	CC17pr
CC17ps	Bt221	CC17pt
CC17pu	Bt222	CC17pv
CC17pw	Bt223	CC17px
CC17py	Bt224	CC17py
CC17na	Bt225	CC17pz
CC17qa	Bt226	CC17qb
CC17qc	Bt227	CC17qd
CC17qe	Bt228	CC17qf
CC17qg	Bt229	CC17qh
CC17qi	Bt230	CC17qj
CC17qk	Bt231	CC17ql
CC17qm	Bt232	CC17qn
CC17qo	Bt233	CC17qp
CC17qq	Bt234	CC17qr
CC17qs	Bt235	CC17qt
CC17qu	Bt236	CC17qv
CC17qw	Bt237	CC17qx
CC17qy	Bt238	CC17qy
CC17na	Bt239	CC17qz
CC17ra	Bt240	CC17rb
CC17rc	Bt241	CC17rd
CC17re	Bt242	CC17rf
CC17rg	Bt243	CC17rh
CC17ri	Bt244	CC17rj
CC17rk	Bt245	CC17rl
CC17rm	Bt246	CC17rn
CC17ro	Bt247	CC17rp
CC17rq	Bt248	CC17rr
CC17rs	Bt249	CC17rt
CC17ru	Bt250	CC17rv
CC17rw	Bt251	CC17rx
CC17ry	Bt252	CC17ry
CC17na	Bt253	CC17rz
CC17sa	Bt254	CC17sb
CC17sc	Bt255	CC17sd
CC17se	Bt256	CC17sf
CC17sg	Bt257	CC17sh
CC17si	Bt258	CC17sj
CC17sk	Bt259	CC17sl
CC17sm	Bt260	CC17sn
CC17so	Bt261	CC17sp
CC17sq	Bt262	CC17sr
CC17ss	Bt263	CC17st
CC17su	Bt264	CC17sv
CC17sw	Bt265	CC17sx
CC17sy	Bt266	CC17sy
CC17na	Bt267	CC17sz
CC17ta	Bt268	CC17tb
CC17tc	Bt269	CC17td
CC17te	Bt270	CC17tf
CC17tg	Bt271	CC17th
CC17ti	Bt272	CC17tj
CC17tk	Bt273	CC17tl
CC17tm	Bt274	CC17tn
CC17to	Bt275	CC17tp
CC17tq	Bt276	CC17tr
CC17ts	Bt277	CC17tt
CC17tu	Bt278	CC17tv
CC17tw	Bt279	CC17tx
CC17ty	Bt280	CC17ty
CC17na	Bt281	CC17tz
CC17ua	Bt282	CC17ub
CC17uc	Bt283	CC17ud
CC17ue	Bt284	CC17uf
CC17ug	Bt285	CC17uh
CC17ui	Bt286	CC17uj
CC17uk	Bt287	CC17ul
CC17um	Bt288	CC17un
CC17uo	Bt289	CC17up
CC17uq	Bt290	CC17ur
CC17us	Bt291	CC17ut
CC17uu	Bt292	CC17uv
CC17uw	Bt293	CC17ux
CC17uy	Bt294	CC17uy
CC17na	Bt295	CC17uz
CC17va	Bt296	CC17vb
CC17vc	Bt297	CC17vd
CC17ve	Bt298	CC17vf
CC17vg	Bt299	CC17vh
CC17vi	Bt300	CC17vj
CC17vk	Bt301	CC17vl
CC17vm	Bt302	CC17vn
CC17vo	Bt303	CC17vp
CC17vq	Bt304	CC17vr
CC17vs	Bt305	CC17vt
CC17vu	Bt306	CC17vv
CC17vw	Bt307	CC17vx
CC17vy	Bt308	CC17vy
CC17na	Bt309	CC17vz
CC17wa	Bt310	CC17wb
CC17wc	Bt311	CC17wd
CC17we	Bt312	CC17wf
CC17wg	Bt313	CC17wh
CC17wi	Bt314	CC17wj
CC17wk	Bt315	CC17wl
CC17wm	Bt316	CC17wn
CC17wo	Bt317	CC17wp
CC17wq	Bt318	CC17wr
CC17ws	Bt319	CC17wt
CC17wu	Bt320	CC17wv
CC17ww	Bt321	CC17wx
CC17wy	Bt322	CC17wy
CC17na	Bt323	CC17wz
CC17xa	Bt324	CC17xb
CC17xc	Bt325	CC17xd
CC17xe	Bt326	CC17xf
CC17xg	Bt327	CC17xh
CC17xi	Bt328	CC17xj
CC17xk	Bt329	CC17xl
CC17xm	Bt330	CC17xn
CC17xo	Bt331	CC17xp
CC17xq	Bt332	CC17xr
CC17xs	Bt333	CC17xt
CC17xu	Bt334	CC17xv
CC17xw	Bt3	

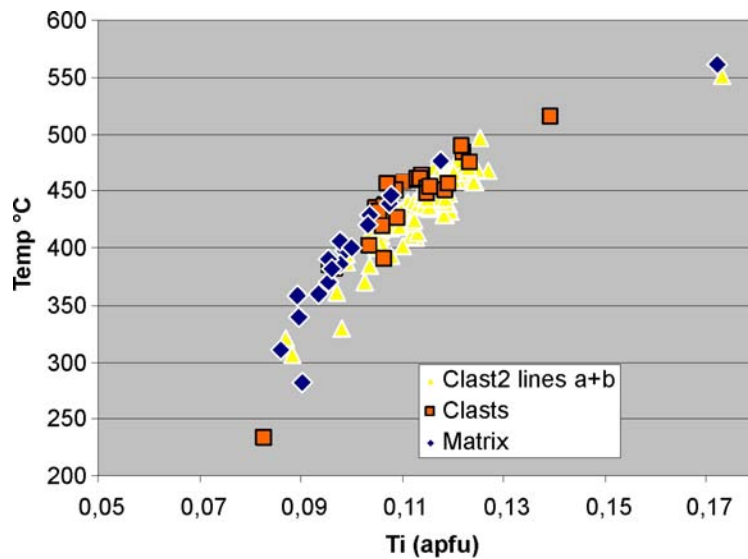


Figure 5.12: Ti vs. temperature for Bt1 (blue rhombi) and Bt2 compositions measured in sample CC17a and calculated after Henry et al. (2005). *Bt1 Clast 2 lines a+b* (yellow triangles) refers to orthogonal profiles measured across the Bt1 clast in Fig. 5.9, with the Ti-content decreasing towards the grain boundaries. Bt1 clast data (orange squares) come from randomly chosen Bt1 clasts floating in the ultramylonitic matrix.

ribbons that characterize most banded mylonites and are themselves displaced by top-SE shear bands. Qtz2 formed by dynamic recrystallization of Qtz1 in the bulging/subgrain rotation (BLG/SGR) regime of Stipp et al. (2002). The grain size of dynamically recrystallized Qtz2 in ribbons from polyphase mylonites is smaller than in pure quartz veins, indicating that the differential stresses were locally significantly higher than the bulk flow stress (see below, cf. Fig. 5.13a&c). Grain boundaries of Qtz2 are slightly bulged and show little evidence for post-D3 static annealing.

Once recrystallization of Qtz1 was completed and all Bt1 transformed into Bt2, Ms2, Chl and Ilm, these phases formed fine-grained (in the order of $\sim 50\mu m$, generally resolvable in light optical microscope) mylonitic layers (Figs. 4.13b, 5.13). The dominant deformation mechanisms in these layers are difficult to infer by the techniques applied. However, the fine grain sizes in polymineralic layers are supporting evidence for a significant contribution of grain-size sensitive deformation mechanism such as viscous grain boundary sliding and pressure solution/precipitation (Fig. 5.13c). As pointed out above, quartz in monophasic aggregates deformed by subgrain

rotation and grain boundary bulging (Fig. 5.13c). Deformation in M-type mylonites may have been accommodated by a combination of intracrystalline plasticity and grain-size sensitive deformation mechanisms in dependence of the composition of the rocks. The observation that these monophase layers are not boudinaged where they form decimeter- to meter-long bands within fine-grained polyphase mylonites (Fig. 5.5) indicates that there is no competence contrast between polyphase and monophase layers and justifies that the rheology of the mylonites is approximated using data determined for pure quartz.

5.4.4 Paleopiezometric data from M-type shear zones

To estimate differential stresses during shear zone networking, we sampled quartz-veins from mature M-type step-over- and host shear zone centers in the juvenile Cala Serena shear zone network (Fig. 5.1, see Fusseis et al. (2006)). Additionally we collected a series of samples along progressively sheared veins from marginal drags to the centers of M-type shear zones (samples CC33a-e and CC15a-d) to investigate the progressive evolution of differential stresses with increasing strain. To determine the grain size of the recrystallized grains, 25 μm thin sections were prepared from wafers cut parallel to the stretching lineation L3 and perpendicular to the foliation S3. In the thin sections domains of dynamically recrystallized Qtz2 were identified and photographed. Between three and ten photographs per sample were rectified to correct them for photographic lens distortions. In each photograph we counted line intercepts along minimum four lines in different orientations (either 90° or 45° apart). From these intercepts, the average grain size for each line was calculated by the mean linear line intercept method and corrected for truncation effects (following Etheridge and Wilkie, 1981, Ord and Christie, 1984, Hacker et al., 1990). Finally, the average grain size for the entire sample was calculated as the arithmetic mean from the sizes of 370-930 grains from 3-10 photographs per thin section. The standard deviation was calculated for each thin section from the corrected grain size data. For calculated grain sizes see table 5.3.

No distinction was made between high- and low-angle grain boundaries, even though we are aware of the nonsystematic error that may falsify our results. However, to determine grain sizes we carefully chose portions of the thin sections that exhibit qualitatively estimated steady state microfabrics

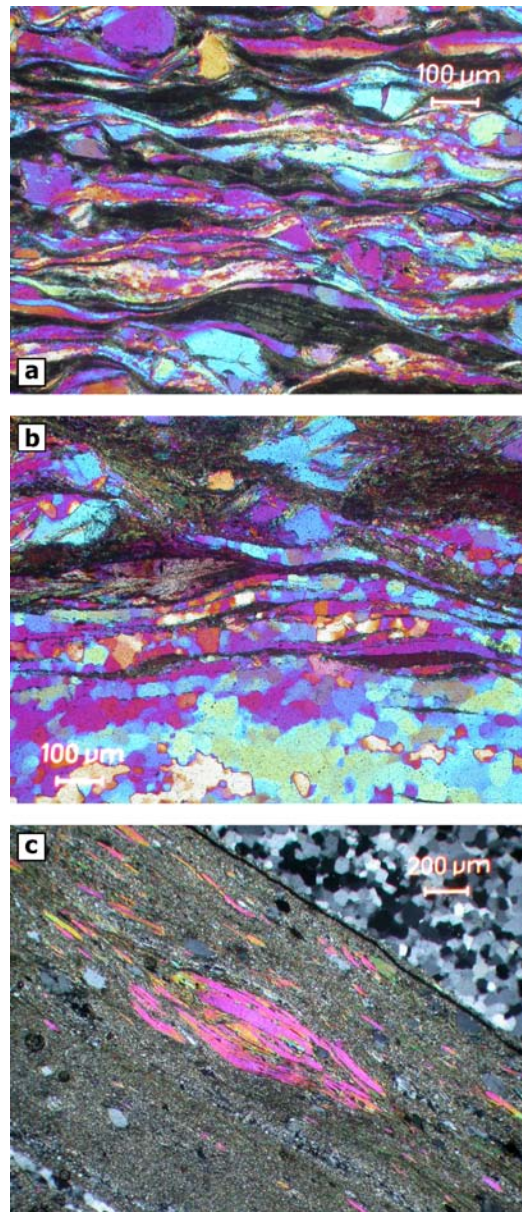


Figure 5.13: Deformation in M-type shear zones. (a) Right-lateral shear bands indicating top-to-SE shear. Note deflected quartz ribbon grains. See text for explanation. Sample CC105. (b) Deformed metapelite. Note quartz, dynamically recrystallizing by subgrain rotation, and reacting Bt1. Sample CC31. (d) Fine-grained polyphase layer next to monophase quartz layer in M-type mylonite. Sample CC52.

formed by dynamically recrystallized grains with high-angle grain boundaries. We believe that we thereby minimized the distortion in the grain size

Sample	Grain size, D (μm)	Differential stress (Mpa)	
		Twiss 1977	Koch 1983
CC33a1xz	67,12±6,33	34,52	24,99
CC33b1xz	76,60±11,03	31,55	20,20
CC33b2yz	65,36±6,08	35,15	26,08
CC33cxz	69,72±8,11	33,64	23,51
CC33dxz	75,48±9,81	31,87	20,69
CC33exz	50,75±6,79	41,75	39,20
CC15axz	88,41±17,66	29,24	16,88
CC15bxz	88,86±15,47	28,52	15,91
CC15dxz	77,92±12,70	31,19	19,66
CC34xz	63,08±10,81	36,01	27,62
CC52xz	89,40±10,92	28,41	15,75
CC101xz	81,29±11,07	30,30	18,36
CC103xz	42,13±4,85	47,38	52,90
CC104xz	118,28±25,56	23,48	10,04
CC106xz	66,18±7,77	34,85	25,57
$\sigma_1 - \sigma_3$ (Mpa) = A*D ⁻ⁿ			
	A	603	21829
	-n	-0,68	-1,61

Table 5.3: Grain sizes and differential stresses in the southern Cala Serena. See text for explanation and Fig. 9.4 in App. 9.5 for sample location.

data caused by low-angle subgrains.

From the arithmetic mean grain size the inferred flow stress - which equals the differential stress, $\sigma_1 - \sigma_3$ - was calculated for each sample (see summarized data in Table 5.3). Following Hacker et al. (1990), we used the recrystallized-grain-size piezometer of Koch (1983), because it is based on data from dry and wet quartzite, flint and novaculite, deformed over a range of pressures, temperatures, and strain rates in different devices. For comparison we included differential stress values calculated using the theoretical piezometer of Twiss (1977). Differential stresses for the rocks in the southern Cala Serena shear zone network range from 19,66 to 52,90MPa, with an average value of 22,33MPa (Table 5.3). No systematic changes characterize samples from step-over and host shear zones (Fig. 5.1).

Interesting to note is that differential stresses determined for the samples from series CC33 do not change significantly along the progressively deformed quartz-vein, ranging from 20,69MPa (lozenge interior, less deformed) to 24,99MPa (shear zone center, highest strains), with the exception of the least deformed sample CC33e (39,20MPa). Recrystallized grains of the latter form by bulging of Qtz1 grain boundaries only. The calculated values

may therefore not represent steady flow stresses but stress concentrations along grain boundaries. However, the determined grain sizes indicate that differential stresses may have been similar from the margins towards the centers of M-type shear zones. The least deformed samples of series CC15 showed to be not suitable for analysis and therefore the samples do not contribute to this statement.

5.5 Discussion

5.5.1 Deformation in UM-type shear zones

UM-type shear zones exhibit several attributes that motivate our interpretation that deformation of the ultramylonites was dominated by grain size-sensitive creep, which is a combination of solid state diffusion (possibly assisted by pressure solution/precipitation) and viscous grain boundary sliding. Our interpretation is motivated by the following arguments:

- We identified a mechanism that produced an ultrafine-grained matrix. The element distribution maps in Fig. 5.9 and 5.10 indicate that the fine-grained ultramylonite resulted from synkinematic reactions of Bt1 and Plag1. The reaction products generally have very fine grain sizes $\ll 15\mu\text{m}$ (Figs. 5.8), which are interpreted to promote viscous grain boundary sliding (e.g. Behrmann, 1985) and are by far smaller than the recrystallized grain size in M-type mylonites (Fig. 5.13).

The neocrystallized reaction products constituted a rheologically weak phase that should have localized strain once isolated reaction sites interconnected and thereby formed a interconnected rheologically weak phase (Fig. 5.11). The relatively homogeneous distribution of Qtz2, Plag2, Bt2 and Ilm, which form the main constituents of the ultramylonite, might be explained by mechanical mixing of reaction products, assisted by selective heterogeneous nucleation of one phase in voids opening during grain boundary sliding between other phases (Figs. 5.8b-d, 5.9, Kruse & Stünitz, 1999, Kenkmann, 2000). The polyphase nature of the ultramylonitic layers hindered grain growth and stabilized the small grain sizes after neocrystallization.

- Lobate outlines and cusps of Bt2/Qtz2 and Bt2/Plag2 phase boundaries evidence a high mobility of phase boundaries (Figs. 5.8b&d),

which is generally explained by diffusive mass transfer (Cumbest et al., 1989, Gower & Simpson, 1992). Viscous grain boundary sliding is generally associated with grain shape modification by diffusion-controlled processes.

- Bt2 forms interconnected load-bearing frameworks in at least parts of all investigated samples. Bt2 in these aggregates lacks evidence for intracrystalline deformation. Lack of, or at least little intracrystalline deformation is regarded as diagnostic for viscous grain boundary sliding (Rutter et al., 1994).

The basal [001] planes of Bt2, which are usually clearly visible in scanning electron microscopy (Fig. 5.8c), show no evidence for bending or kinking. Glide along basal [001] crystallographic planes of aligned Bt2 would induce the formation of shape-preferred orientations of the aggregates and long axes of the deformed grains would appear rotated towards S3. This contradicts our observations; Bt2 grains in all samples form aggregates at arbitrary angles to S3 (Fig. 5.8). Bt2 deformation and grain shape modification may have been accommodated by diffusive mass transfer and precipitation following pressure solution.

- Alignment of isolated Bt2, Plag2 and Ilm promotes the formation of sliding planes on scales larger than individual grains. Such sliding planes were identified in sample CC12a (Fig. 5.8b) and are considered as typical for viscous grain boundary sliding (e.g. White, 1977, Stünitz & Fitz Gerald, 1993, Fliervoet et al., 1997). Alignment of matrix phases (including isolated Bt2 and Ilm), which is a precondition for the formation of sliding planes, may be explained by synkinematic crystallization of the minerals within an applied stress field.

Our interpretation of the investigated fabrics is supported by similar descriptions of ultramylonites from natural shear zones in peridotites (Stünitz, 1998, Newman et al., 1999, Handy & Stünitz, 2002), gabbros (Kruse & Stünitz, 1999, Kenkmann, 2000, Kruse et al., 2001, Kenkmann & Dresen, 2002) and quartzofeldspathic rocks (Kerrick et al., 1980, Behrmann & Mainprice, 1987, Stünitz & Fitzgerald, 1993, Fliervoet et al., 1997, Pennacchioni & Cesare, 1997) whose deformation was dominated by grain-size sensitive creep. Similar to the ones investigated in this paper, most of these ultramy-

lonites formed along retrograde PT-paths at granulite- to greenschist-facies metamorphic conditions by syntectonic reactions and recrystallization of a pre-existing mineral assemblage (cf. Figs. 5.9, 5.10). All of them are characterized by a very fine-grained (generally $<10\mu\text{m}$) polyphase matrix (cf. Fig. 5.8). Extremely fine grain sizes are considered as facilitating viscous grain boundary sliding (Boullier & Gueguen, 1975, Behrmann & Mainprice, 1987), even though they are not a precondition. Porphyroclastic grains in the described shear zones mostly exhibit extensive crystal plastic deformation (e.g. Kruse & Stünitz, 1999, Kruse et al., 2001, Kenkmann & Dresen, 2002) and sometimes fracturing (Handy & Stünitz, 2002), indicating a significant bulk deformation prior to strain localization in ultramylonitic shear zones (cf. Figs. 5.6c, 5.7a&c). Progressive strain localization in ultramylonitic shear zones is often interpreted to have involved a switch from dominantly dislocation creep to grain size sensitive creep mechanisms as the fine-grained reaction products formed an interconnected weak layer (cf. Fig. 5.11, Newman et al., 1999, Kenkmann & Dresen, 2002).

5.5.2 Grain size-sensitive creep in step-over shear zones

The distribution of UM-type shear zones forming step-over shear zones and drag truncations reveals that they were embedded in the shear zone networking process and therefore active coevally with F- and M-type shear zones (Fig. 5.1). Since deformation in UM-type shear zones was dominated by grain size sensitive creep rather than crystal plastic deformation (which dominated deformation in M-type shear zones), the reasons for selective formation of ultramylonites in step-over shear zones and drag truncations need to be explained. To date, we do not have a satisfactory model to explain grain size sensitive creep in drag truncations, but in the following we will propose a model that explains why grain size sensitive creep in UM-type shear zones was activated where M-type shear zones interconnected laterally and describes the inferred evolution of UM-type shear zones during the homogenization of strain distribution within the shear zone network.

Progressive shear zone networking was described by Fousseis et al. (2006, see their section 4.2 and Fig. 14): First, host shear zones formed as shear fractures which propagated and interconnected longitudinally. After accumulating a critical displacement they developed a mylonitic shear zone center (Fousseis & Handy, Chapter 4 of this thesis). To reduce strain en-

ergy and to deform compatibly host shear zones interconnected laterally by forming step-over shear zones and thereby isolated sigmoidal lozenges of less-deformed host rock. Due to bulk simple shear deformation, step-over shear zones rotated synthetically and caused lozenges to deform internally by compartmentalization and shear zone widening. As step-over shear zones became parallel to the bulk shearing direction, lozenges were incorporated into the mylonitic shear zones and deformation was homogenized within the initial limits of the shear zone network.

As discussed above, we interpret the ultramylonitic matrix in UM-type shear zones to result from the reactions of Bt and Plag. The reaction of Bt was identified in the ductile tip damage zone of a propagating M-type shear zone, where (shear) stresses locally rose above (i.e. positively deviate from) the remote level (Fusseis & Handy, Chapter 4 of this thesis). These retrograde, potentially stress-driven reactions have been described by Kerrich et al. (1980, 1981). Shear stress deviation fields (sSDFs) typically occur at the tips of shear fractures and, less pronounced, mylonitic shear zones (e.g. Pollard & Segall, 1987, Barr & Houseman, 1992, Medvedev, pers. comm. 2005). The dimension of these fields is a function of the viscosity contrast between shear zone and host rock. Around shear zones (mode II shear fractures or mylonitic shear zones deforming by simple shear) in mechanically isotropic rocks sSDFs are symmetric about the shearing plane and show an increase in shear stresses around the shear zone tips.

In our interpretation, S1/2, which represented a pronounced mechanical anisotropy (Fusseis & Handy, Chapter 4 of this thesis), influenced the exact shape of the sSDFs around host shear zones. S1/2 deflected propagating shear fractures, which were precursors in the tip damage zones of mylonitic shear zones, antithetically (Fig. 5.14a, see discussion in Fusseis & Handy, Chapter 4 of this thesis). This deflection is interpreted to have shifted the sSDFs at the tips of the propagating shear zone (Fig. 5.14a). sSDFs of shear zones in a parallel array interact if the combined dimension of the sSDFs exceeds the lateral distance of the shear zones (e.g. Nicholson & Pollard, 1985, Handy & Streit, 1999, Mancktelow, 2005) which might have been the case between host shear zones in parallel arrays (Fig. 5.14b). Shear zone tips that were antithetically deflected by S1/2 and propagated far enough to meet their counterparts approaching from a parallel shear zone on a nearby shearing plane defined the initial orientation of step-over shear

zones (Fig. 5.14a, Füsseis & Handy, Chapter 4 of this thesis). The combined effects of deflection of propagating fractures by S1/2 and interacting SDFs were therefore responsible for the sigmoidal-shaped lozenges that characterize shear zone networks at the Cap de Creus (Fig. 5.14b, Carreras, 2001).

Interaction of stress deviation fields was shown to cause a deflection of tips of propagating extension veins (Nicholson & Pollard, 1985, Handy & Streit, 1999) and linkage of propagating shear fractures (Lin & Logan, 1991). An increase in shear stress within the interacting sSDFs at the Cap de Creus might therefore have been able to locally accelerate the bulk mylonitic overprint of the rock (Füsseis & Handy, Chapter 4 of this work). Increased shear stresses might have caused brittle fracturing of the rock, which is evidenced by brittle terminations of UM-type shear zones. Brittle failure would have promoted an increased fluid flow, which is indicated by extensional veins in Plag1 filled with newly grown Bt2. Increased availability of fluids would have enhanced reactivity of Bt1 and Plag1 and enabled an effective redistribution of chemical components in the reacting rock to form the ultramylonitic layers. The ultramylonites that were found along unsheared lithological boundaries parallel to nearby step-over shear zones may indicate that the increase in shear stress alone was sufficient to trigger reactions of Bt and Plag (Fig. 5.3c).

Once step-over shear zones formed, bulk deformation was partitioned among step-overs and host shear zones. Lozenges that were isolated from their host by surrounding shear zones started to rotate synthetically. Since shearing was found to have been isochoric (Füsseis et al., 2006) these movements should have caused high differential stresses along step-over shear zones (Fig. 5.14c). Such high differential stresses are expressed in extremely fine grain sizes of dynamically recrystallized Qtz2 ($\ll 50\mu\text{m}$) in monophasic layers within UM-ultramylonites (Fig. 5.7c). High stresses promoted high strain rates and therefore high rates of heterogeneous nucleation of grains in the ultramylonitic matrix (Stünitz, 2006, pers. comm.). Consequently, the grain sizes of narrow (millimeter-wide) juvenile polyphase ultramylonites are small ($<10\mu\text{m}$, Figs. 5.8b&d). Constant volume, compatible deformation and the rotation of step-over shear zones in a bulk simple shear regime (cf. Füsseis et al., 2006) required the lozenges to deform internally (inset in Fig. 5.14c). The rotation of step-over shear zones is interpreted to have caused

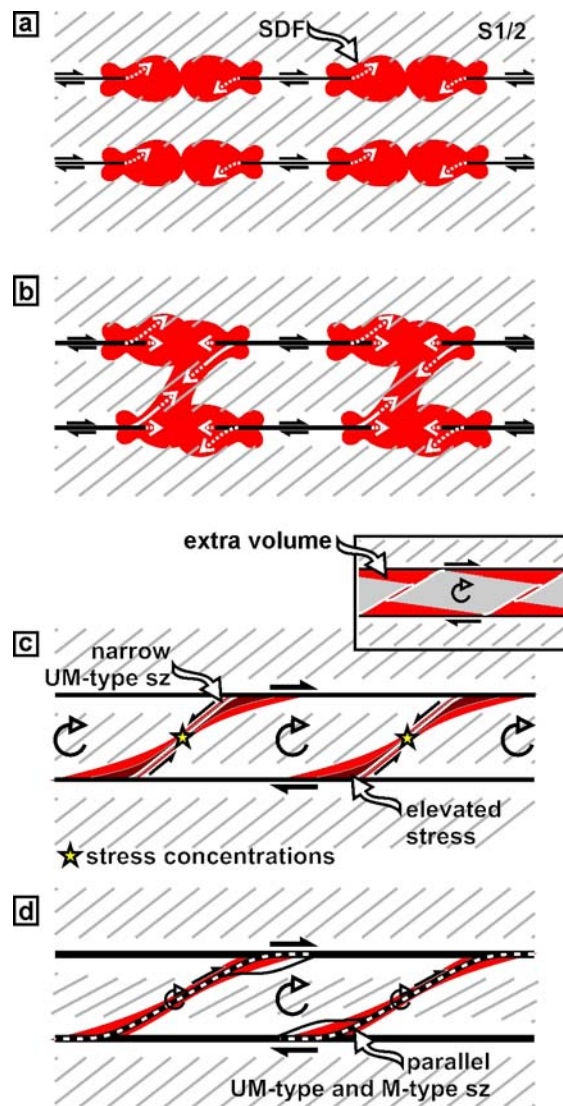


Figure 5.14: Model for the formation of UM-step-over shear zones: (a) Array of parallel propagating (host) shear zones with asymmetric stress deviation fields (SDFs, red - positive deviation compared to bulk shear stress). Black solid lines - M-type shear zones, white dotted lines - F-type shear zones, grey solid lines - S1/2. (b) Interacting SDFs. White solid line - UM-type shear zones. (c) Networked UM- and M-type shear zones. Red and dark-red areas indicate elevated stresses due to the lozenge's tendency to rotate clockwise. (d) Central lozenge starts to compartmentalize to deform compatibly (see inset in (c)). Black and white stippled lines indicate the dominance of dislocation creep over grain-size sensitive creep in mature step-over shear zones. See text for explanation.

stress concentrations in the upper left and lower right corner of the lozenges (dark red fields in Fig. 5.14c), which is where lozenge compartmentalization commenced (Fig. 5.1, fig. 10 in Fousseis et al., 2006).

Within the shear zone network, widening of both, host- and step-over shear zones was coeval to a pronounced mylonitic overprint of the neighboring lozenges. Both effects increased the deforming rock volume and thereby relaxed strain rates along step-over shear zones. Reduced strain rates decreased the rate of heterogeneous nucleation within ultramylonitic UM-type shear zones and allowed the ultramylonites to coarsen, explaining larger matrix grains ($>10\mu\text{m}$) in polyphase ultramylonites from centimeter-wide UM-type shear zones (Figs. 5.4b, 5.8c). By widening, ultramylonitic layers in step-over shear zones became part of M-type shear zones, which constitute the widest step-over- and host shear zones (e.g. figs. 12 & 13 in Fousseis et al., 2006). Deformation in these, with respect to UM-type shear zones, coarser grained mylonites is interpreted to have involved a combination of deformation mechanisms, largely dependent on the composition of the deforming rock. Qtz2 deformed by dislocation creep in the GBB/SGR regime of Stipp et al. (2002), Bt2 by glide parallel to basal [001] crystallographic planes and pressure solution/precipitation. Fine-grained polyphase aggregates are interpreted to have deformed by grain size sensitive creep (Figs. 4.13b, 5.13b&c). Within widening step-over shear zones, ultramylonitic layers may have continued deforming, however, most of the displacement was then accommodated by surrounding M-type mylonites (Fig. 5.13c).

5.6 Summary and Conclusions

We investigated the contribution of different deformation mechanisms to the formation of decameter-wide mylonitic shear zones that constitute the kilometer-scale Northern Shear Belt at the Cap de Creus, NE Spain. In the following we will summarize our observations in a model for the evolution of these decameter-wide shear zones which formed from arrays of isolated meter-long mylonitic shear zones parallel to the bulk shearing direction that interconnected and homogenized strain within the enclosed rocks.

Isolated parallel mylonitic 'host' shear zones interconnected across their shearing direction through the formation of brittle 'step-over' shear zones oriented up to $\sim 80^\circ$ to the bulk shearing direction. Propagation of these step-over shear zones was strongly influenced by a pre-existing foliation at high angles to the host shear zones (Fusseis & Handy, see Chapter 4 of this thesis). Shear zone interconnection allowed partitioning of strain and promoted the formation of a shear zone network. During shear zone networking, fractures were precursors to thin ultramylonitic shear zones. The extremely fine-grained (5-15 μm) polyphase matrix of these ultramylonitic shear zones resulted from the synkinematic, potentially stress-driven reactions of biotite and plagioclase to form biotite, muscovite, ilmenite, quartz, plagioclase and garnet. Within the ultramylonitic layers, the roughly homogeneous mineral phase distribution, lobate phase boundaries between biotite and quartz/feldspar, lacking evidence for intracrystalline deformation and the formation of transgranular sliding planes indicate that deformation in the ultramylonites was dominated by diffusion-assisted solution/precipitation and viscous grain boundary sliding. Thermometric data determined from newly grown garnet and biotite indicate syndeformational temperatures of 400-500°C. Extremely small grain sizes of dynamically recrystallized monophase quartz layers in step-over shear zones together with the selective formation of ultramylonites in these orientations suggest that step-over shear zones were subjected to elevated stresses. We explain this elevated stresses by strain compatibility problems that arouse as step-over shear zones bounding relatively rigid sigmoidal lozenges of country rock rotated towards the host shear zones in overall simple shear deformation. Isochoric compatible deformation caused the lozenges to deform internally during this process. This internal deformation commenced along the lozenge's margins by widening of the bounding shear zones. Widening of step-over and host

shear zones involved pronounced crystal plastic deformation of the adjacent country rock. Thereby, the deforming rock volume increased and the stresses within host-, but also step-over shear zones, decreased. The grain size of dynamically recrystallized quartz in monophasic layers increased to equilibrate to an average differential stress of 22,3 MPa. During shear zone widening, the extremely fine-grained ultramylonitic layers in step over shear zones remained existent within a mylonitic host rock. In these decimeter- to decameter-wide mylonitic shear zones most of the displacement was accommodated by crystal plastic deformation of dynamically recrystallized quartz and newly grown aggregates of biotite, as well as grain size sensitive creep in fine-grained ($\sim 50\mu m$) polyphase aggregates of quartz, biotite, muscovite, chlorite and ilmenite resulting from the decay of primary biotite in the mylonitic layers. As step-over shear zones rotated towards the bulk shearing direction and thereby, as less-deformed country rock in the lozenges became progressively incorporated into the shear zones, strain distribution was homogenized within the shear zone network and a decameter-wide mylonitic shear zone formed.

5.7 Acknowledgements

We thank Matthias Konrad-Schmolke and Claudio Rosenberg for stimulating discussions and reviews of earlier versions of the manuscript that helped to improve the paper. Matthias Konrad-Schmolke is furthermore thanked for his assistance in doing the microprobe analyses. Holger Stünitz is thanked for fruitful discussions. Furthermore we thank Sarah Hauten and Susanne Schneider for their assistance during preparation of the manuscript. We acknowledge the support of the Cap de Creus national park authorities for issuing a permit to collect rock samples in the park and thank Jordi Carreras for his help. This work was funded by DFG project Ha 2403/6.